Journal Pre-proof

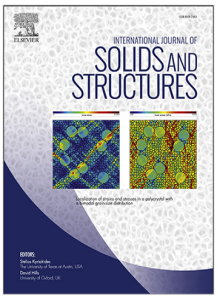

In-plane pipe whip: Post-failure dynamic response

D. Schiano Moriello, F. Bosi, R. Torii, P.J. Tan

PII: S0020-7683(22)00330-4
DOI: https://doi.org/10.1016/j.ijsolstr.2022.111860
Reference: SAS 111860

To appear in: *International Journal of Solids and Structures*

Received date : 25 April 2022
Revised date : 6 June 2022
Accepted date : 12 July 2022

Please cite this article as: D. Schiano Moriello, F. Bosi, R. Torii et al., In-plane pipe whip: Post-failure dynamic response. *International Journal of Solids and Structures* (2022), doi: https://doi.org/10.1016/j.ijsolstr.2022.111860.

In-plane pipe whip: post-failure dynamic response

D. Schiano Moriello[a], F. Bosi[a,*], R. Torii[a], P.J. Tan[a]

[a]*Department of Mechanical Engineering, University College London, London, WC1E 6BT, UK*

Abstract

Pressurized pipes are ubiquitous in chemical, nuclear and power plants. A sudden failure and release of high-speed fluid cause large inelastic displacements characterized by a whipping-type motion, which can ultimately hinder the surrounding structural and functional systems. In this paper, a beam user element has been developed, implemented and applied to analyze the in-plane flexural dynamic response of pipe whip. The two-dimensional Euler-Bernoulli beam element is based on the corotational kinematic formulation and elastoplastic constitutive models that include metal plasticity and moment-curvature relationships obtained from numerical bending tests, which highlighted the existence of two new dimensionless groups that govern the flexural response of slender pipes and enable the creation of moment-curvature master curves for thick and thin pipes. The corotational beam element formulation is compared against an analytical rigid-perfectly plastic model, numerical simulations employing shell elements and available experimental results, showing very good accuracy in the prediction of the inelastic deformation response of pipe whip and its hazardous area of influence. Furthermore, parametric studies are performed to investigate the effect of load intensity, cross-sectional geometry and concentrated tip mass on the post-failure deformation modes, plastic hinge formation and extension of the hazard zone. The presented results represent valid tools to assess the safety of industrial piping systems undergoing failure, and to optimally design pipe whip restraints.

Keywords: Corotational framework, Pipe rupture, Damage, Plastic hinges, Steel pipes

1. Introduction

Thin-walled pipes are structural elements that offer manifold fields of engineering applications, from gas and liquid transportation systems to chemical, nuclear and power plants. The prediction of the dynamic inelastic response of pipes is of paramount importance to assess the safety of industrial systems when a failure occurs, and to design appropriate restraints. In particular, if a pipe transporting pressurized fluids experiences an accidental release of the internal fluid, the high-speed fluid jet will cause the pipe to undergo large displacements in a dynamic whipping-type motion. The schematic of a pipe whip problem

*Corresponding author

Email addresses: dario.schiano.15@ucl.ac.uk (D. Schiano Moriello), f.bosi@ucl.ac.uk (F. Bosi), r.torii@ucl.ac.uk (R. Torii), pj.tan@ucl.ac.uk (P.J. Tan)

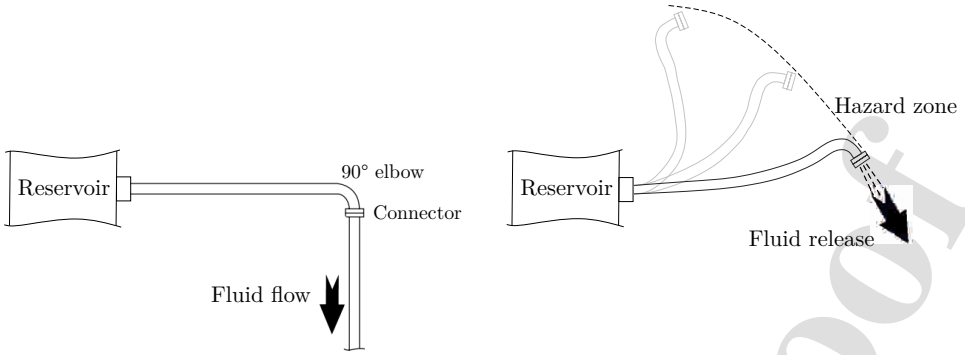

Figure 1: Schematic of pipe whip break, where a pipe transporting pressurized fluid experiences a sudden failure at the connector (left), thus releasing a high-speed fluid jet that causes the pipe to deform in a dynamic whipping-type motion (right). The hazard zone, which represents the area of influence of the pipe after failure, is reported as a dashed line.

following a sudden guillotine break is presented in Fig. 1, where the fluid jet generates an intense loading, causing the initially intact pipe to deform at high speed. Hence, pipe whip constitutes a serious hazard due to the likelihood of impacting nearby structures and causing extensive damage to equipment, structural or functional components [1, 2]. To increase the safety of the system, pipe whip restraint devices are installed, which absorb the kinetic energy of the pipe before it damages neighbouring structures. Despite the improved safety, the installation of restraints can severely reduce access to the system, thus compromising the performance of maintenance operations.

With the aim of optimising the number of restraints and the design of piping systems, pipe whip motion has been studied in detail [3, 4]. The R3 Impact Assessment Procedure [5, 6] and the code ANSI/ANS 58.8 [7] have been used to assess the hazards of pipe rupture. Baum conducted an experimental investigation on steel pipes to understand the influence of pipeline geometry and fluid pressure on in-plane pipe whip [8]. For each experiment, the study measured the hazard zone, which is the extent of the area of influence of the pipe after its failure and release of high-pressure fluid. Stronge and Yu [9] developed a theoretical rigid-perfectly plastic model for predicting the collapse of slender structures in bending, later applied to the analysis of in-plane pipe whip where the fluid jet is modelled through a follower impulsive force [10, 11]. The model predicts with satisfying accuracy the hazard zone of pipe whip when additional mass, such as that of a flange or connector, is not present. However, when the mass is significant, it underestimates the plastic hinge position. Subsequent upgrades to the model were made to include inelastic and strain-hardening effects [3].

The advancements of computing technology have enabled the development of numerical models to analyze the deformation of pipe whip. Reid et al. [3] created a finite difference model for in-plane pipe whip,

employing non-linear constitutive laws that simulate metal plasticity and the bending behaviour of pipes. The framework predicted with accuracy the response of relatively thick pipes, but was less successful for thin pipes, when the deformation is dominated by the collapse of the cross-section. Finite element analyses employing shell elements were performed to assess the hazard zone and the cross-sectional collapse mechanisms, at the expense of computational time due to the need for a sufficiently refined mesh. Micheli and Zanaboni [12] used pipe elements to obtain conservative predictions of the whip motion and reduce the computational time. However, pipe elements (sometimes referred to as elbow elements [13]) have shown limited reliability in capturing the cross-sectional collapse mechanism [14], while beam-general-section elements show excessive collapse when employed to simulate thin pipes [13].

Inspired by the aforementioned research, and to overcome the limitations of the currently available elements, a novel beam element is here developed for modelling pipes undergoing in-plane large deformations. The element employs an elastoplastic hardening-softening constitutive model for bending, predicting with great accuracy pipes deformation, the hazard zone and the development of plastic hinges. The formulation has a significantly reduced computational cost, compared to shell element analyses. It relies on the corotational kinemetic framework, which enables the decomposition of motion into rigid-body and pure deformational counterparts. One of the first corotational finite element models is attributed to Belytschko and Hsieh [15], who developed beam and triangular shell elements for transient small-strain analyses and noticed that the evaluation of the strains in the deformed frame increases the computational speed by simplifying the governing equations. Later, Crisfield et al. [16, 17] developed a consistent corotational formulation for beam, shell and solid elements, where the stiffness matrix transformation is consistent with that applied to the force vector. Felippa and Haugen [18] framed a unified small-strain theory for corotational elements in static analyses, noting that a consistent stiffness matrix can be equilibrated and symmetrisable, thus allowing the use of Newton solvers without loss of quadratic convergence. Le et al. [19, 20] framed the theory of elastoplastic corotational beam elements in two-dimensional and three-dimensional dynamic analyses, employing a consistent mass matrix to obtain high levels of accuracy and stability even with a coarse mesh. Their framework was later extended to consider contact analyses for planar elements [21].

The paper is organised as follows: the corotational framework for beam elements and the elastoplastic constitutive relations are presented in Sect. 2, where moment-curvature master curves are developed for thick and thin pipes. The analytical rigid-perfectly plastic model for the dynamic response of pipe whip subjected to follower force and tip mass is derived in Sect. 3. The numerical implementation of the developed corotational beam element subroutine is reported in Sect. 4 alongside its validation against experiments from the literature and FE analyses employing shell elements. Finally, the numerical results are discussed in Sect. 5, where the predictions of parametric studies are presented to show the influence of load intensity, cross-sectional geometry and concentrated tip mass on the deformation modes, plastic hinge formation and extension of the hazard zone.

2. Corotational beam element framework and constitutive modelling

A beam user element has been developed to predict the flexural dynamic response of slender pipes and it has been implemented in the finite element software Abaqus v2018 (Dassault Systèmes) through a user element subroutine (VUEL). The beam model is based on the corotational kinematic formulation to ensure fast convergence and provide a rapid, yet accurate, tool that overcomes the limitation of currently available beam element formulations and reduces the computational time required when shell elements are employed. Using the corotational framework enforces material-frame indifference and consents to use non-linear constitutive models for the relation between local rotations and cross-sectional moments based on experimental observations from bending tests performed on pipes [22]. Furthermore, the method involves a reduction of the number of degrees of freedom when operating in the local frame, which contributes to the model's simplicity and has the potential to reduce the computational cost. A corotational beam element is developed following the approach of Felippa and Haugen [18] and Le et al. [19], Sect. 2.1, where the constitutive models include metal plasticity and moment-curvature master curves obtained from numerical simulation of bending tests on thick and thin pipes, Sect. 2.2.

2.1. 2D Euler-Bernoulli corotational beam element

The formulation of a user-defined 2D beam element within the corotational framework follows the approach of Felippa and Haugen [18] in the definition of the local strains, and that of Le et al. [19] in the definition of the mass matrix and a transformation matrix that is not limited to small rotations. Assuming slender circular pipes with a ratio between length L and diameter D greater than 15, the Euler-Bernoulli beam theory is used. In this study, pipes with hollow circular cross-section and a slenderness ratio $L/D > 60$ are considered. Under these assumptions, bending is the predominant deformation mode and the effect of transverse shear can be safely neglected from the corotational formulation.

The corotational framework for a planar beam with two nodes is presented visually in Fig. 2. Each node is identified in the global reference frame by the coordinates $(x_i, y_i)_{i=1,2}$ and it is assigned with three degrees of freedom: the horizontal and vertical displacements, u_i and w_i, and the rotation θ_i. The deformation vector and its associated internal force vectors are

$$\begin{aligned} \mathbf{u} &= \{u_1, v_1, \theta_1, u_2, v_2, \theta_2\}^{\mathsf{T}}, \\ \mathbf{f} &= \{F_{x,1}, F_{y,1}, M_1, F_{x,2}, F_{y,2}, M_2\}^{\mathsf{T}}, \end{aligned} \tag{1}$$

where $\{\ \}^{\mathsf{T}}$ indicates the transpose operator. The beam's initial configuration is defined by the rotation angle β_0 and the element length l. Upon deformation, a corotated frame $\mathbf{C}^R$ that moves rigidly with the element can be defined through the angle β, Fig. 2. The local frames $\mathbf{C}_1^D$ and $\mathbf{C}_2^D$ are introduced to separate the deformational and rigid components of motion. They follow the rotation of each node, with local orientations $\bar{\theta}_1$ and $\bar{\theta}_2$ with respect to the frame $\mathbf{C}^R$. The motion decomposition allows for arbitrarily

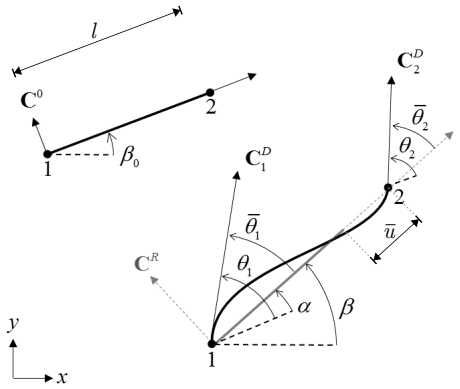

Figure 2: Reference frames for a planar beam element with two nodes. The Cartesian coordinates (x, y) define the global reference frame, and $\mathbf{C}^0$ is the initial configuration of the element. At any time increment, $\mathbf{C}^R$ identifies the current corotated reference frame, whereas $\mathbf{C}_1^D$ and $\mathbf{C}_2^D$ the deformed configuration at each node.

large rotations at each end, provided that a sufficiently small number of elements is employed [19]. Hence, the local deformation vector and its associated local force vector can be written as

$$\begin{aligned} \bar{\mathbf{u}} &= \left\{\bar{u}, \bar{\theta}_1, \bar{\theta}_2\right\}^{\mathsf{T}}, \\ \bar{\mathbf{f}} &= \left\{\bar{N}, \bar{M}_1, \bar{M}_2\right\}^{\mathsf{T}}. \end{aligned} \tag{2}$$

The components of the local deformation vector $\bar{\mathbf{u}}$ are

$$\begin{aligned} \bar{u} &= l_n - l = \sqrt{(x_2 + u_2 - x_1 - u_1)^2 + (y_2 + v_2 - y_1 - v_1)^2} - \sqrt{(x_2 - x_1)^2 + (y_2 - y_1)^2}\,, \\ \bar{\theta}_i &= \theta_i - \alpha = \theta_i - \beta + \beta_0\,, \quad i = 1, 2\,, \end{aligned} \tag{3}$$

where l and l_n are the lengths of the element in the undeformed and deformed configuration, respectively, $\alpha = \beta - \beta_0$ represents the rigid rotation, and the angles β_0 and β can be evaluated from the nodal coordinates $(x_i, y_i)_{i=1,2}$ and displacements $(u_i, v_i)_{i=1,2}$.

The components of the local force vector are the axial force $\bar{N}$, determined through the element elongation, and the bending moments $\bar{M}_i$ associated with the rotations $\bar{\theta}_i$. These components can be evaluated once the local deformation vector $\bar{\mathbf{u}}$ is defined, based on the definition of the local nominal strain $\varepsilon = \bar{u}/l$. Hence, the axial force is $\bar{N} = \sigma A_n$, where $\sigma = \sigma(\varepsilon)$ is the stress acting on the cross-section along the longitudinal direction, which depends on the opportune choice of a constitutive model (Sect. 2.2), and A_n is the current cross-sectional area, obtained through incompressibility assumption from the initial cross-section A. The corotational element employs the Euler-Bernoulli beam theory to evaluate the curvature in the local reference frame, with the Hermitian shape functions [19]

$$S_1 = \bar{x}\left(1 - \frac{\bar{x}}{l}\right)^2, \qquad S_2 = -\left(1 - \frac{\bar{x}}{l}\right)\frac{\bar{x}^2}{l}, \tag{4}$$

where $\bar{x}$ is the local coordinate along the longitudinal axis. The curvature k is then expressed as a function of $\bar{x}$ as

$$k(\bar{x}) = \frac{\partial^2}{\partial \bar{x}^2}\left[S_1\bar{\theta}_1 + S_2\bar{\theta}_2\right] . \tag{5}$$

The element formulation is completed by the specification of a constitutive law relating the bending moment at the nodes, $\bar{M}_i$, to the curvatures k_i, as described in Sect. 2.2.

In the corotational framework, the expression of the force vector, $\mathbf{f}$, is obtained by noting that the element internal energy is independent of the reference frame and through the principle of virtual work as $\mathbf{f} = \mathbf{B}^{\mathsf{T}}\bar{\mathbf{f}}$, where the transformation matrix $\mathbf{B}$ is defined as

$$\mathbf{B} = \frac{\partial \bar{\mathbf{u}}}{\partial \mathbf{u}} = \begin{bmatrix} -c & -s & 0 & c & s & 0 \\ s/l_n & -c/l_n & -1 & -s/l_n & c/l_n & 0 \\ -s/l_n & c/l_n & 0 & s/l_n & -c/l_n & 1 \end{bmatrix} , \tag{6}$$

where $c = \cos\beta$ and $s = \sin\beta$.

The explicit solution algorithm to be used for dynamic analyses requires the definition of a mass matrix, which was chosen as a lumped mass matrix to reduce the computational cost [13, 19]:

$$\mathbf{M} = \frac{\rho A l}{2}\,\mathrm{diag}\left\{1, 1, \frac{l^2}{12}, 1, 1, \frac{l^2}{12}\right\}, \tag{7}$$

where ρ is the density. The first two terms on the diagonal, corresponding to the displacement degrees of freedom, are obtained by dividing the total mass of the element between the two end nodes, whereas the third term, which corresponds to the rotational degree of freedom, represents the inertia of a rigid rod that is rotating about its centre of mass. Finally, the user element subroutine requires a stable time increment for the explicit integration algorithm, which was chosen as [13]

$$\Delta t = f\sqrt{\frac{\rho\, l\, l_n}{E}}\,, \tag{8}$$

where E is Young's modulus and f is a small multiplicative factor that ensures the satisfaction of the Courant-Friendrichs-Lewy (CFL) condition [23]. The value of f was found through an iterative process when modelling the deformation of pipewhips. When f is close to unity, the overestimation of the stable time increment leads to instability in the solution algorithm, which is evidenced by excessive element distortions. By decreasing f, the algorithm stabilises at the expense of the computational time. The optimum range was found in the interval $f = 0.2$–0.01 where the algorithm retains stability whilst keeping the solution time shorter than 2 min.

2.2. Constitutive model and moment-curvature master curves

The stress-strain response employed to define the material constitutive model is representative of ductile metals, characterised by an elastic phase, followed by strain hardening until necking is reached, after which

the material is modelled as perfectly plastic [3]. In the material subroutine, described in Sect. 4.1, the strain hardening phase is discretized through a piece-wise linear approximation with kinematic hardening assumption. The material considered is mild steel, with model parameters that followed the experimental characterisation and investigation of circular pipes carried out by Reid et al. [3].

Additionally, the bending behaviour of the pipe must be modelled through the definition of moment-curvature ($M-k$) relationships. The typical flexural behaviour of circular pipes is characterised by an initial linear elastic regime up to the yield point, (M_Y, k_Y), followed by a hardening phase up to the maximum point (M_C, k_C) and a softening region that terminates with failure, (M_F, k_F), after which the bending moment is assumed constant for increasing values of curvature [8, 3]. Similarly to the stress-strain response, the moment-curvature relation is approximated through a piece-wise linear model and expressed as [24]

$$M(k) = \begin{cases} M^E(k) = EIk\,, & |k| < k_Y \\ M^{HS}(k) = \text{sign}(k)\left(M_i + \dfrac{M_{i+1}-M_i}{k_{i+1}-k_i}|k-k_Y|\right), & |k| \geq k_Y\,, |k| < k_F \\ M^F(k) = \text{sign}(k)M_F\,, & |k| \geq k_F \end{cases} \tag{9}$$

where I indicates the second moment of area of the pipe cross-section and the index i denotes the points of the curve discretisation.

Considering the limited number of experimental data for the definition of the moment-curvature relation for circular pipes [25, 26], numerical simulations were performed to investigate the bending response of pipe with different cross-section geometries. Several combinations of external diameter D and wall thickness H were analysed, Table 1. The chosen dimensions are based on the standards ASTM A312M, ASME B36.19M-2004, ASTM A106M and ASME B36.10M-2004. The nomenclature used to distinguish thick (Pi) from thin (TPi) pipes follows the Mariotte's formula for cylinders under pressure, where $D/H = 20$ denotes the critical ratio. When $D/H \leq 20$, a pipe is considered relatively thick, and an overall uniform ovalization in bending is expected. On the contrary, when $D/H > 20$, the pipe is considered thin, and displays pronounced cross-sectional collapse. Please note that the nomenclature of thin and thick pipe is referred to the ratio between the diameter and the cross-sectional thickness, while the slenderness ratio remains $L/D > 60$, thus justifying the use of Euler-Bernoulli beam model.

Table 1: Typical values of outside diameter D and wall thickness H for stainless steel and carbon steel pipes.

Pipe	P1	P2	P3	P4	P5	P6	TP1	TP2
D (mm)	48.3	48.3	48.3	42.2	33.4	48.3	48.3	42.2
H (mm)	2.77	3.68	5.08	2.77	2.77	3.18	1.65	1.65
D/H (-)	17.4	13.1	9.5	15.2	12.1	15.1	29.3	25.5

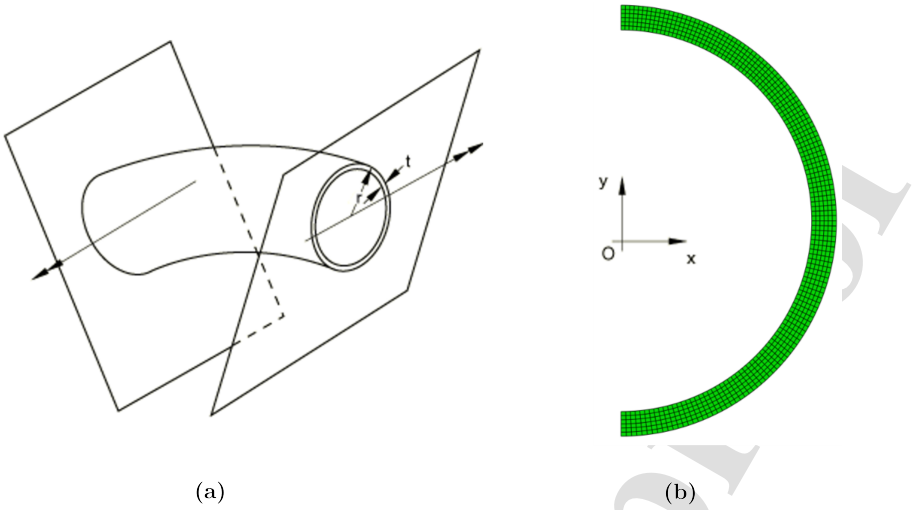

(a) (b)

Figure 3: Simulation setup for the Riks analysis for the determination of the moment-curvature relationship. (a) prescribed rotation imposed at two rigid walls to generate constant curvature and bending moment, and (b) example of discretisation of the pipe cross-section with generalised plane strain elements.

The deformation of a pipe in bending is a strongly non-linear problem due to the ovalization and eventual structural instability leading to the collapse of the cross-section as the rotation increases. Hence, a Riks analysis was performed, and considering the pipe's high slenderness and the assumption that plane sections remain planar after deformation, the static response in bending can be studied using a generalised plane strain model. A unit length of a pipe, straight in its undeformed configuration, was bounded by two rigid walls, where an increasing rotation was prescribed to induce constant bending and curvature, as illustrated in Fig. 3(a). One half of the pipe cross-section is discretised using 4-nodes generalised plane strain elements with reduced integration (CPEG4R) and a minimum of six elements along the thickness, with symmetry conditions prescribed, as in Fig. 3(b). The elements are allowed to distort in plane, and have an additional degree of freedom in the out-of-plane direction, tied to the relative rotation of the walls with respect to a reference point. The material considered was mild steel and the stress-strain curve was taken from the experiments performed by Reid et al. [3], shown in Fig. 7(b), with metal plasticity fitted through the Johnson-Cook power law model, $\bar{\sigma} = a + b\bar{\varepsilon}^n$, where $\bar{\sigma}$ and $\bar{\varepsilon}$ are the equivalent stress and strain, respectively. The material parameters are reported in Table 2.

The moment-curvature relations extracted from the simulation of bending tests are displayed in Fig. 4(a). The moment was obtained by integrating the stresses acting in the out-of-plane direction on the cross-section, whereas the curvature is calculated from the relative rotation imposed on the bounding planes. The figure shows that thick pipes, labelled Pi, are characterised by an extended hardening region, followed by negligible

Table 2: Material properties used in the numerical bending tests on mild steel pipes.

ρ	E	ν	σ_Y	a	b	n
(kg/m^3)	(GPa)	-	(MPa)	(MPa)	(MPa)	-
7850	200	0.33	295	266.1	530.5	0.5608

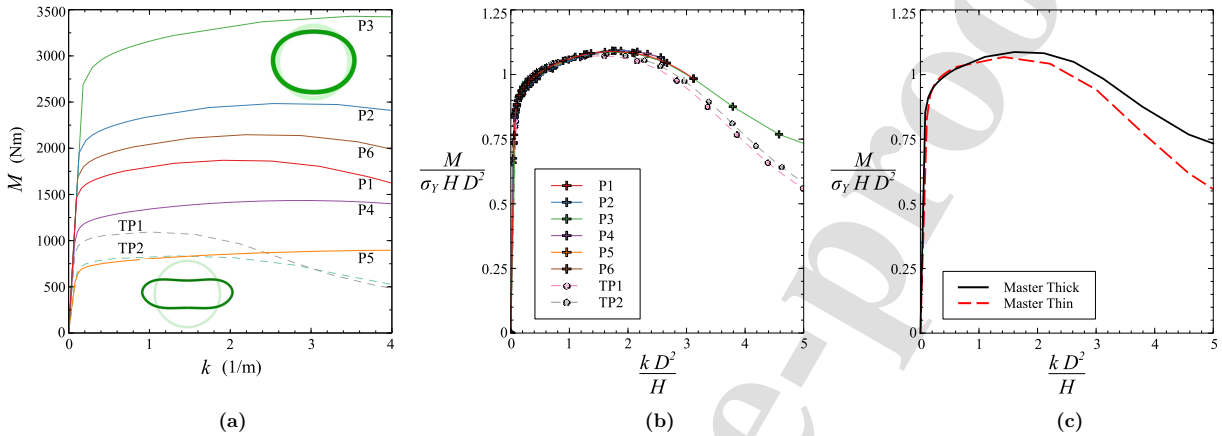

Figure 4: Moment-curvature relations obtained from the numerical bending tests on mild steel pipes. Dimensional (a) and dimensionless (b) relations for thick (Pi, solid curves) and thin (TPi, dashed curves) pipes with cross-sectional geometries defined in Table 1. The insets show the undeformed (light green) and deformed (green) cross-sections for thick (top) and thin (bottom) circular pipes, respectively. (c) Dimensionless moment-curvature master curves for thick (—) and thin (– –) pipes.

softening, whereas the curves for thin pipes, labelled TPi, are distinguished by a short hardening region, followed by a lengthy softening branch. The insets report the cross-sectional deformation of the pipes P1 and TP1. Despite the small difference in wall thickness, the pipes display completely different behaviours when subjected to the same loading, with the geometry TP1 exhibiting a noticeable collapse, while P1 shows a uniform ovalization. Furthermore, each dimension of the cross section leads to a different response, not monotonically related to the ratio D/H. Therefore, a dimensional analysis using Buckingham's theorem was performed to identify the parameters affecting the shape of the moment-curvature curves. It was found that the flexural behaviour of the pipes is completely identified by three dimensionless groups

$$\pi_1 = \frac{D}{H}\,, \qquad \pi_2 = \frac{M_c}{\sigma_Y H D^2}\,, \qquad \pi_3 = \frac{k_c D^2}{H}\,, \tag{10}$$

where the parameters $M_c = M_c\left(\sigma_Y, D, H\right)$ and $k_c = k_c\left(\sigma_Y, D, H\right)$ identify the maximum point in the M-k curves.

Rearranging the M-k curves of Fig. 4(a) with the dimensional groups π_2 and π_3, it is possible to ob-

tain relations of dimensionless moment, $M/(\sigma_Y H D^2)$, versus dimensionless curvature, $k\,D^2/H$, as shown in Fig. 4(b). It can be seen that the dimensionless curves tend to overlap in the elastic and hardening phase, up to the maximum point. Beyond this point, two different behaviours can be distinguished, where thin pipes exhibit a more pronounced softening phase compared to thick pipes. Based on these observations, two master curves can be defined, Fig. 4(c). The advantage of establishing these master curves is that they are independent of the yield strength and cross-section dimensions, so that they can be used to define the moment-curvature relationship for thin and thick pipes. In this study, the master curves will be employed when experimental data from the literature are not available. To the best of the authors' knowledge, the definition of the dimensionless groups π_2 and π_3, and of the master curves for describing the behaviour of pipes in bending have not been previously reported in the literature, which suggested that ad-hoc experimental or numerical studies should be performed for each cross-sectional geometry [25, 26, 27].

It should be noted that, at the current stage, the constitutive model neglects the strain rate effects and the interaction between tensile and flexural components in the definition of the yield surface. Furthermore, the study only considers pipes with circular cross-section. The derivation of similar M-k curves and their experimental validation should be considered for future investigations.

3. Analytical model

This section presents analytical solutions for the dynamic response of cantilever beams constituted on rigid-perfectly plastic (RPP) material. These simplified closed-form solutions provide a valuable tool to quickly assess the deformation mechanisms, comparing them with the finite element response through the developed corotational user element.

When a cantilever beam of length L is loaded at its free end with a concentrated follower force F oriented orthogonally to the beam's longitudinal axis (see inset of Fig. 5), its response depends on the magnitude of the force with respect to the critical force that causes plastic hinge formation at the fixed end, $F_C = M_P/L$ [9, 28]. In particular, the beams exhibits three behaviours depending on the dimensionless force $f = F/F_C$: (**i**) if $f < 1$, the beam remains stationary, (**ii**) if $f \in [1, 3]$, it rotates about the fixed end, where the plastic hinge forms, while (**iii**) if $f > 3$, the beams rotates about a plastic hinge that develops along the beam length. The length of the plastic hinge is approximately equal to the pipe's external diameter. When $f > 1$, the beam deforms dynamically with a mechanism that is influenced by the loading intensity and pulse shape. Assuming a constant force $f_0 = F_0/F_C$, from the translational and rotational equations of motion it was demonstrated that a plastic hinge forms at a dimensionless distance [9]

$$\lambda = \frac{3}{f_0} \tag{11}$$

from the beam free end, and it only depends on the load intensity. Hence, the beam's hazard zone ζ (i.e. the maximum extent of the area of influence of the pipe after failure) can be approximated by the hinge

position, $\zeta \approx \lambda$ [24]. Solving the equations of motion for the case of a load intensity that changes over time, $f = f(t)$, leads to [9]

$$\lambda = \frac{3\tau}{p(\tau)}\,, \qquad p(\tau) = \int_0^\tau f(\tilde{\tau})\,\mathrm{d}\tilde{\tau} \tag{12}$$

where $\tau = t/t_0$ is the dimensionless time, t the time, $t_0 = L\sqrt{\rho/F_C}$ a characteristic time and $p(\tau)$ the pulse intensity. From Eq. (12) it can be deduced that, once formed, a plastic hinge will move towards either end of the beam with a velocity

$$\dot{\lambda} = \frac{\mathrm{d}\lambda}{\mathrm{d}\tau} = \frac{3}{p(\tau)^2}[p(\tau) - \tau f(\tau)]\,. \tag{13}$$

The evolution of the tip force $f(\tau)$ determines the sign of $\dot{\lambda}$. The hinge will be stationary for $\dot{\lambda} = 0$, it will move towards the fixed end for $\dot{\lambda} > 0$ when the loading decreases over time, and will move towards the free end for $\dot{\lambda} < 0$ when the loading is increasing.

Stronge and Yu [9] further studied the RPP model for a cantilever beam hit by a falling object of mass m. If the coefficient of restitution is null (i.e. the mass stays attached to the beam after the impact), the position of the plastic hinge can by determined by

$$\lambda = \frac{1}{2\,\gamma\,v_0}\left(3\tau + \sqrt{9\tau^2 + 24\gamma^2 v_0 \tau}\right), \tag{14}$$

where $\gamma = m/(\rho A L)$ is the dimensionless mass, ρ the material density of the beam, A the cross-sectional area and v_0 its initial dimensionless velocity.

Stronge and Yu [9] did not investigate the case of beams loaded with a follower tip force and simultaneously hit by a travelling mass at the free end. The extension of the RPP model to this particular case, assuming null coefficient of restitution, initial dimensionless velocity v_0 of the mass and a generic force pulse shape $p = p(\tau)$, can be obtained through the translational and rotational equations of motion in dimensionless form

$$\begin{cases} \dfrac{1}{2}\lambda v = \gamma(v - v_0) + p\,, \\[2ex] \dfrac{1}{6}\lambda^2 v = \tau. \end{cases} \tag{15}$$

where $v = v(t)$ is the post-impact dimensionless velocity of the free-end. Solving the system of equations gives the hinge position $\lambda = (\tau, \gamma, v_0)$ as a function of time, the relative mass and initial velocity,

$$\lambda = \frac{1}{2(\gamma v_0 + p(\tau))}\left(3\tau + \sqrt{9\tau^2 + 24\gamma^2 v_0 \tau + 24\gamma p(\tau)\tau}\right). \tag{16}$$

Substituting $v_0 = 0$ gives the hinge position for a cantilever beam loaded with a concentrated follower force and an initially static mass at its tip

$$\lambda = \frac{1}{2p(\tau)}\left(3\tau + \sqrt{9\tau^2 + 24\gamma p(\tau)\tau}\right). \tag{17}$$

In the limit of $\tau \to 0$, Eq. (17) provides the initial hinge position

$$\lambda_0 = \frac{1}{2f_0}\left(3 + \sqrt{9 + 24\gamma f_0}\right). \tag{18}$$

This analytical solution can be applied to the case of pipe whip, where the load is generated by the sudden release of a high pressure fluid. The intensity of the blow-out force is initially determined by the reservoir's pressure, and gradually decays over time as the pipe deforms. According to the experimental observations from Reid et al. [3], the force is extinguished when cross-sectional collapse causes the obstruction of the fluid flow, otherwise, the force decays to a stationary value. It is suggested that in the case of pipe whip the force pulse can be substituted with a linearly decaying pulse of the type [3, 9]

$$f = \begin{cases} f_0\left(1 - \dfrac{\tau}{\tau_D}\right) & \tau < \tau_D\,, \\ 0 & \tau \geq \tau_D\,, \end{cases} \tag{19}$$

where τ_D is the pulse duration in dimensionless unit. The pulse intensity then becomes

$$p(\tau) = \begin{cases} f_0\tau\left(1 - \dfrac{\tau}{2\tau_D}\right) & \tau < \tau_D\,, \\ f_0\tau_D/2 & \tau \geq \tau_D\,. \end{cases} \tag{20}$$

Substituting the relations above in Eqs. (12) and (17), it is possible to obtain an explicit expression for the variation of the hinge position over time in pipe whip

$$\lambda(\tau) = \frac{3}{f_0(1 - \tau/2\tau_D)}\,, \tag{21}$$

and in the case of a pipe with a concentrated dimensionless tip mass γ

$$\lambda(\tau, \gamma) = \frac{3 + \sqrt{9 + 24\gamma f_0(1 - \tau/2\tau_D)}}{2f_0(1 - \tau/2\tau_D)}. \tag{22}$$

The curves predicted by Eqs. (21) and (22) are plotted in Fig. 5 for a linearly decaying pulse. A pulse duration of $t_D = 0.68$ s ($\tau_D = 3.97$) was chosen to reflect the typical pulse duration observed in the experimental studies on pipe whips [3]. In the figure, solid lines represent the hinge location predicted at $\tau = 0$, whereas dashed lines indicate the hinge position at $t = 0.2$ s ($\tau = 1.17$). The dimensionless mass $\gamma = 0.2$ was used, which corresponds to that of the pipe whip experiments from Reid et al. [3], typical of the mass of the flange or connector that fails and causes the release of the fluid in an industrial environment.

4. Numerical implementation and validation

4.1. User element VUEL architecture

The architecture of the developed corotational beam element subroutine VUEL, and its location within the explicit solution procedure, is illustrated in Fig. 6. At any increment, for each finite element, the explicit

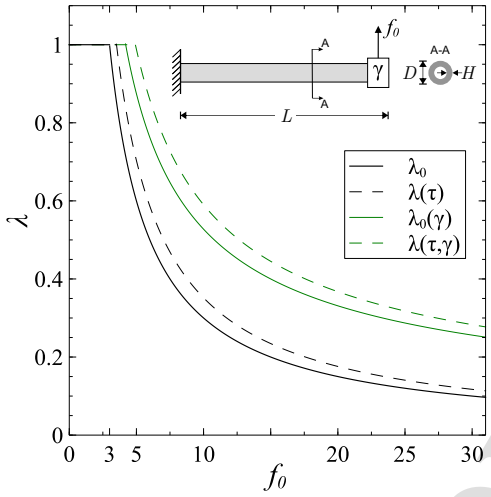

Figure 5: Theoretical predictions of plastic hinge position, λ, for pipe whip subjected to a linearly decaying force pulse of initial intensity f_0. The black lines labelled λ_0 and $\lambda(\tau)$ are obtained through Eqs. (18) and (21), and indicate the hinge position at the time $t = 0.0$ s and $t = 0.2$ s, respectively. The green lines $\lambda_0(\gamma)$ and $\lambda(\tau, \gamma)$ are obtained through Eqs. (18) and (22), and indicate the response predicted at the same instants for pipe whip with a concentrated mass at the tip, $\gamma = 0.2$. The inset shows the schematic of the cantilever slender pipe of length L, cross-section dimensions D, H and dimensionless tip mass γ subjected to a dimensionless follower force f_0.

solution algorithm provides the current nodal coordinates (x_i, y_i), and the translational and rotational degrees of freedom associated with each node, u_i, v_i, θ_i, $i = 1, 2$. The scope of the user element is to evaluate the internal force vector $\mathbf{f}$ and the mass matrix $\mathbf{M}$ necessary to solve Newton's equation and evaluate the state of the element at the end of the increment. In particular, the corotational framework first transforms the displacement vector from the global to the local reference frame, $\mathbf{u} \rightarrow \bar{\mathbf{u}}$ through Eq. (3). Then, the material module is called to evaluate the components of the local force vector, $\bar{\mathbf{f}}$, starting from the axial local strains ε and curvatures k_i, Eq. (5), and employing the constitutive models of Sect. 2.2. Lastly, the corotational framework converts the forces back to the global reference frame, $\bar{\mathbf{f}} \rightarrow \mathbf{f}$ through the transformation matrix $\mathbf{B}$, Eq. (6), before the accelerations $\ddot{\mathbf{u}}$ and nodal displacements $\mathbf{u}$ are obtained by inverting Newton's law. The next time increment Δt is then computed by means of Eq. (8).

4.2. Validation of the VUEL code

The developed corotational beam element was validated by comparing its numerical predictions with the finite element simulations and experiments performed by Reid et al. [3] to determine the in-plane flexural response of pipe whip.

The numerical model reproduces the experimental apparatus and it is constituted of a straight pipe of length L, external diameter D and thickness H with a flange of mass m at one end. Two pipe geometries

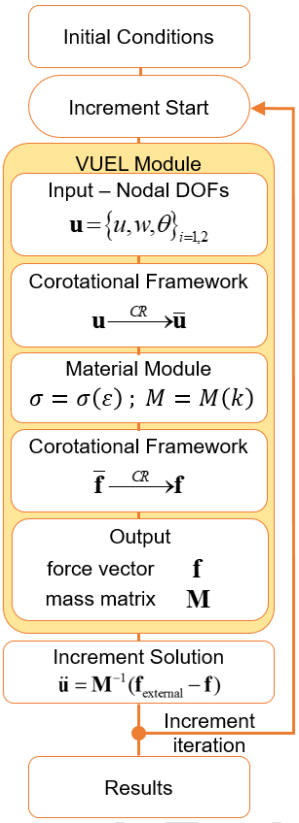

Figure 6: Schematisation of a dynamic FEA solution algorithm, which includes the main architecture of the developed corotational beam element VUEL module.

were considered, representative of thick (labelled as $V1$) and thin (labelled as $V2$) pipes, respectively, as reported in Table 3. The pipe was modelled as a cantilever beam clamped at one end, with a concentrated mass at the free end subjected to a concentrated follower force of initial intensity F_0. The load intensity varies over time following the force pulse measured during the experiments of Reid et al. [3], Fig. 7(a), causing the pipe to deform in plane. It should be noted that the intensity of the load gradually decreases during the motion of the pipe due to its progressive cross-sectional collapse that reduces the fluid flow.

The pipe was made of mild steel, with material properties reported in Table 2. Metal plasticity is modelled following the approach described in Sect. 2.2; the strain-hardening behaviour is included in the analysis as tabular data discretising the plastic stress-strain curve of the material reported in Fig. 7(b). Similarly, the constitutive relation between bending moment and curvature, which depends on the cross-sectional dimensions of each pipe, is included as tabular data discretising the experimental M-k curves shown in Fig. 7(c).

The simulations were carried out in Abaqus/explicit using the developed user elements. A mesh conver-

Table 3: Values of pipe dimensions, initial force intensity and flange mass used in the experimental tests on in-plane pipe whip performed by Reid et al. [3].

Test case	D (mm)	H (mm)	D/H -	L (m)	F_0 (kN)	m (kg)
$V1$	50.8	2.60	19.5	3.00	11.25	1.80
$V2$	50.8	1.58	32.2	2.73	11.25	1.04

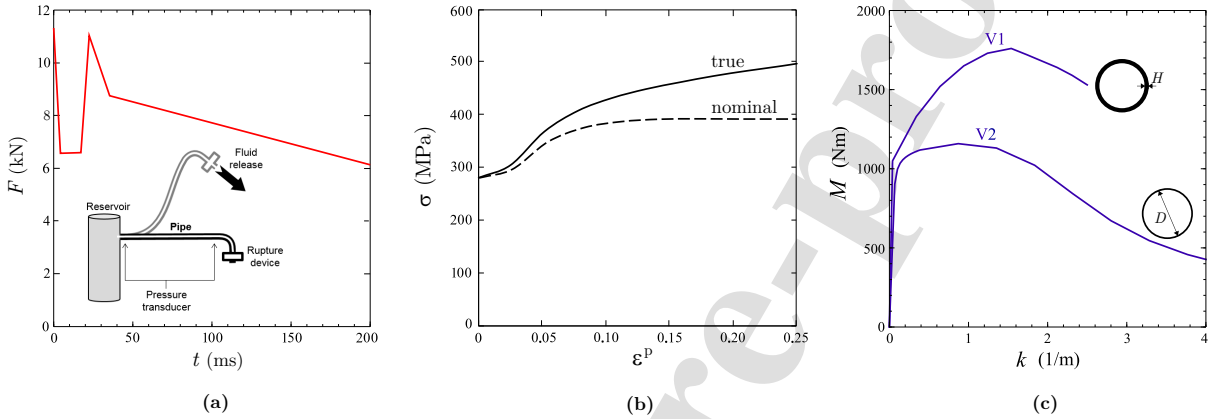

Figure 7: (a) Force pulse measured in the test of in-plane pipe whip. (b) True (solid) and nominal (dashed) stress vs. plastic strain from uniaxial tensile tests on mild steel employed in the simulation of pipe whip. (c) Moment-curvature curves for geometries $V1$ and $V2$ used in the simulation of in-plane pipe whip. The data are extracted from the experiments on in-plane pipe whip performed by Reid et al. [3], while the inset shows the schematisation of their experimental apparatus.

gence study proved that 20 beam elements were sufficient to capture the deformation of the pipes with a maximum error of 2% with respect to the reference solution obtained with 100 elements.

Figure 8(a) shows the deformation history of the relatively thick pipe of the test case $V1$ ($D/H = 19.5 < 20$) as predicted by the simulation using VUEL elements. The results are compared with the experimental (label Exp) and numerical (label Num) results of Reid et al. [3]. As stated in the experimental observations [3], the pipe undergoes continuous bending, and there is no discernible kinking of the pipe, which would correspond to localised cross-sectional collapse. Both numerical models predict well the instantaneous deformation profile of the pipe. The maximum relative error for the position of the free end, between our simulation and the experimental data, is observed at the 60 ms time frame and is smaller than 3.5%. The agreement with the experimental data confirms that both numerical models are suitable for the simulation of large plastic deformation of thick-walled pipes. The small discrepancy in the deformation profiles between

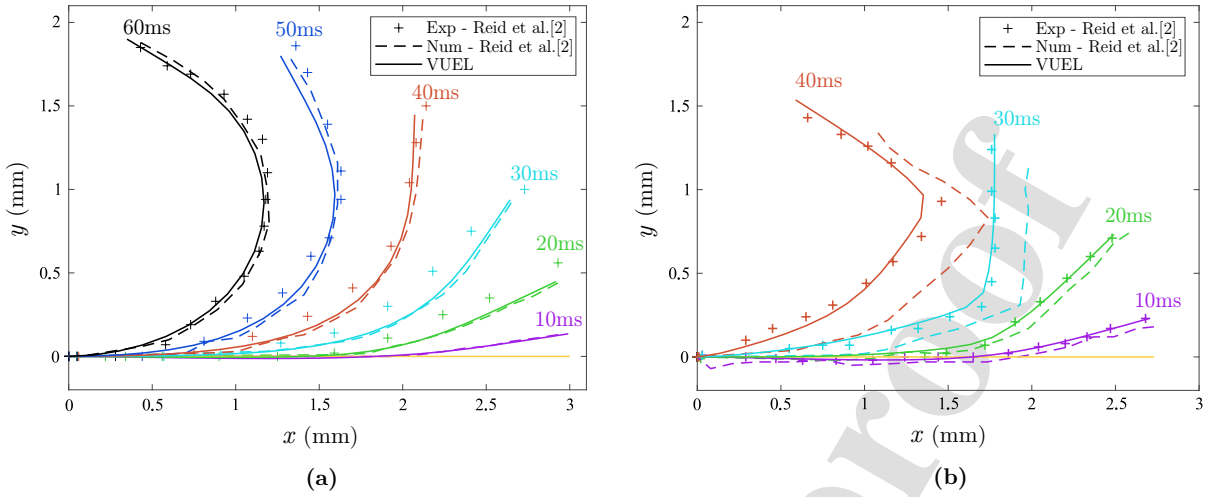

Figure 8: Deformed shapes of the pipe whip from the test case $V1$ (a) and $V2$ (b) at several time frames. The simulations results obtained with the VUEL beam element code (—) are compared with the experimental results (Exp, +) and numerical predictions (Num, – –) from Reid et al. [3].

both numerical solutions and the experimental results at early time frames might be attributed to the approximation of the initial part of the force pulse.

The results of the study on the thin pipe $V2$ ($D/H = 32$) are presented in Fig. 8(b). According to the experimental observations, most of the deformation was localised in a small region at $x \approx 1.7$ m, where complete cross-sectional collapse was observed, starting at 30 ms. Subsequently, the deformation progresses with the rotation of the pipe about the fixed end. Very similar behaviour was observed with the VUEL simulation. In the first 20 ms, the pipe starts bending, with the centre of rotation located at $x \approx 1.7$ m. In the following time frames, the pipe continues to bend around this point, while the second centre of rotation forms at $x = 0$. The comparison with the experimental measurements in Fig. 8(b) shows that the user element subroutine captures well the time and the position where localisation occurs, with a maximum relative error for the position of the free end measured at 40 ms which is smaller than 5%. It is worth noticing that the numerical study by Reid et al. [3] predicts with less accuracy the evolution of the deformation profile, which could be due to the finite difference scheme employed in their study.

The agreement with the experimental data confirms that the developed corotational user element VUEL is capable of accurately predicting the large deformation of thick and thin slender pipes. It also captures the locations of maximum curvature, which correspond to localised mechanisms of cross-sectional collapse observed experimentally.

4.3. Comparison with shell elements and rate-dependent material model

In order to complete the validation of the user element, and evaluate the computational efficiency, the numerical results are obtained for a thin pipe with $D/H = 32$, where $D = 50.8$ mm and $H = 1.58$ mm. The predictions from the model employing VUEL elements are compared with those obtained using standard shell elements (type S4R) on an equivalent model run through Abaqus/explicit. The cross-section discretization comprises 40 shell elements with an aspect ratio 1, so the final mesh is composed of 27360 shell elements.

Fig. 9(a) and (c) show that there is reasonably good agreement between the two models in terms of plastic hinges location λ_i and hazard zone ζ. The maximum relative difference for λ_1 was 6% measured at $f_0 = 15$ in Fig. 9(a), and for ζ was 35% at $f_0 = 10$ in Fig. 9(c), and the two models have similar deviations from the theoretical predictions obtained through Eqs. (18) and (21). When comparing the results from the two models, one must take into account the limitations of the beam model, which is only able to capture the deformation of the longitudinal axis of the pipe, whilst the cross-sectional collapse is modelled through the moment-curvature constitutive relation. On the other hand, the usage of shell elements allows for a structural representation of the cross-section, which can directly influence the deformation profile [29, 30].

Additionally, the results from a model employing shell elements and a strain-rate dependent constitutive behaviour are plotted in Fig. 9(b) and (d). The strain rate dependence was added to the previously employed rate-independent material model by using the Cowper-Symonds model, where $D = 40.4\ \mathrm{s}^{-1}$ and $q = 5$ define the rate dependency for mild steel [31, 32]. There is in general negligible difference in results when strain-rate effects are considered, especially when comparing the hazard zone. The only substantial deviation was observed for λ_2 at $f_0 = 20$, where the high strain-rate causes an increase in the distance of the secondary plastic hinge from the free end.

The comparison of the running time between the corotational user beam elements and standard shell formulation testifies the computational efficiency of the developed framework. In particular, the completion time for two simulations with a timestep of 45ms and the same output frequency are: 31 s with VUEL elements, 45 min and 36 s with shell elements, or 4 min and 39 s with shell elements when 12 parallel units are used to speed-up the simulation. Therefore, a simulation employing VUEL elements is reportedly 88 times faster than an analogous shell-elements simulation, and 9 times faster than the same simulation employing 12 parallel units.

5. Results and discussion

The corotational beam user element subroutine was employed in Abaqus/explicit to investigate the effect of the pipe geometry and load intensity on the dynamic response of pipe whip. The analytical model of Sect. 3 shows that the dimensionless hazard zone, ζ, and plastic hinge location, λ, depend on two dimensionless groups: the loading intensity $f_0 = F_0 L/M_P$ and the mass ratio $\gamma = m/(\rho A L)$. Hence, assuming a linearly

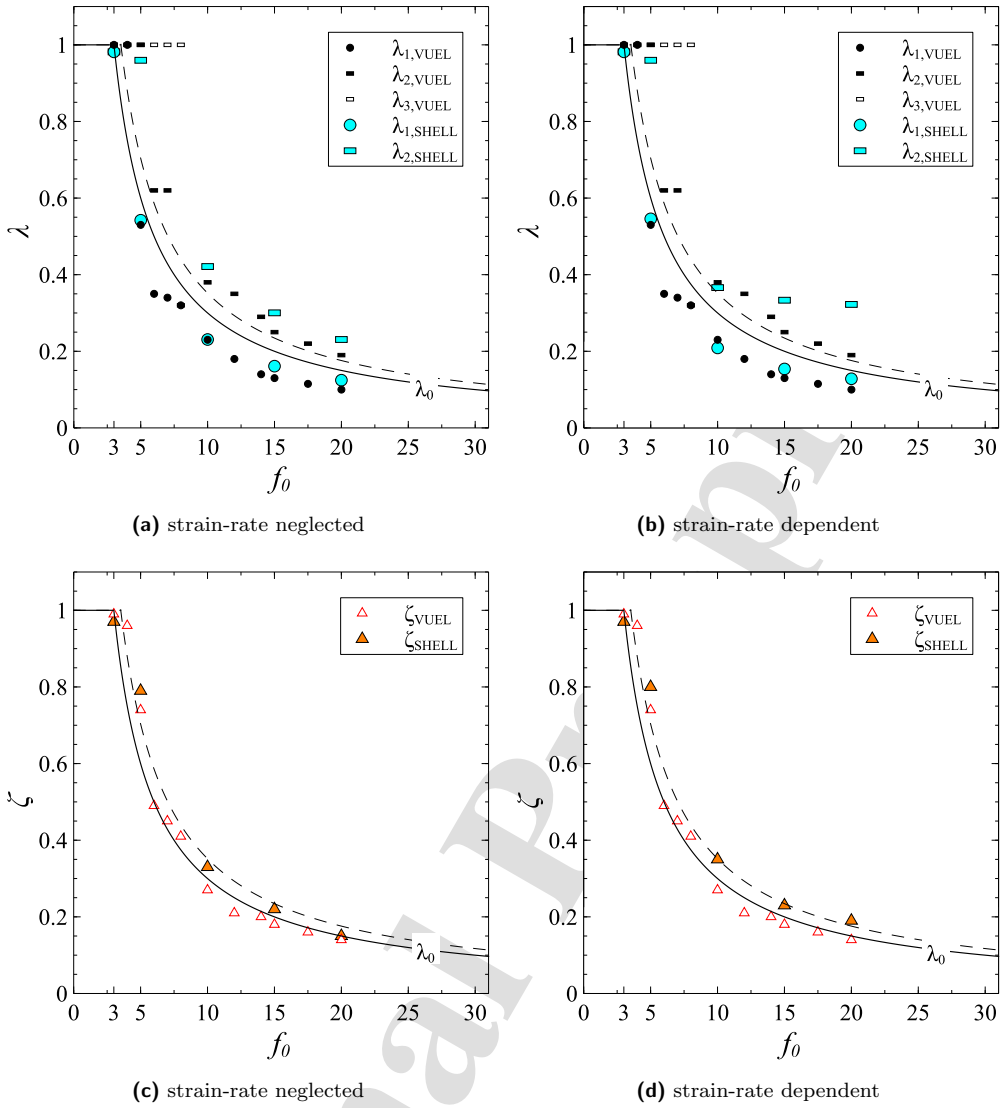

(a) strain-rate neglected

(b) strain-rate dependent

(c) strain-rate neglected

(d) strain-rate dependent

Figure 9: Plastic hinges location λ_i (a,b) and hazard zone ζ (c,d) reported as a function of the dimensionless applied force f_0 for the numerical simulations of pipe whip with $D/H = 32$ using VUEL elements and shell elements. (a,c) Results for strain-rate independent material response and (b,d) for shell elements with strain-rate dependent constitutive model. The solid (—) and dashed (– –) curves represent the analytically-derived hinge position λ at time $t = 0.0$ s (λ_0) and $t = 0.2$ s, respectively.

decaying force with $\tau_D = 3.97$, expressed by Eq. (19), parametric studies were here conducted to analyse the influence of the parameters F_0, L, m and M_P.

The pipes have fully-constrained boundary conditions at the fixed end, referred to as the pipe's root, and are loaded at the opposite end with a concentrated follower force that is initially orthogonal to the

Table 4: Values of pipe dimensions, plastic moment and collapse force for the first parametric study on pipe whip, in which the load intensity varies in the range $f_0 \in [3, 30]$.

Test case	D (mm)	H (mm)	D/H	L (m)	M_P (kNm)	F_C (kN)
$T1$	50.8	2.60	20	3.00	0.220	0.733
$T2$	50.8	1.58	32	2.73	0.133	0.486
$T3$	508.0	12.70	40	10.0	1046	104.6

pipe's longitudinal axis. Although it was shown that a mesh of 20 beam elements is sufficient to capture the free-end displacement of the pipe whip, a finer mesh of 80 elements is here employed to analyse in more detail the location and extension of plastic hinges. The elements employ the moment-curvature relationships obtained in Sect. 2.2, and the same material properties for mild steel there described. For each cross-section characterised by the external diameter D and wall thickness H, the plastic moment M_P is defined as [33, 8]

$$M_P = \frac{4}{3}\left[\left(\frac{D}{2}\right)^3 - \left(\frac{D}{2} - H\right)^3\right]\sigma_Y \alpha\,, \tag{23}$$

with

$$\alpha = \left(1 - \frac{\sigma_U}{\sigma_Y}\right)\frac{D}{80H} + \frac{\sigma_U}{\sigma_Y}\,, \tag{24}$$

where α is a strain-hardening factor depending on the yield stress $\sigma_Y = 279$ MPa and the ultimate stress $\sigma_U = 392$ MPa.

5.1. Effect of load intensity and cross-sectional geometry

The first parametric study analyses the deformation of pipes with two different combinations of cross-sectional dimensions to investigate the response of thick and thin pipes. The pipes dimensions are reported in Table 4 and correspond to those of the pipe whip from the experimental investigation of Reid et al. [3] (cases $T1$ and $T2$), and one representative of the typical dimensions of a pipeline employed for petrochemical applications [34] (case $T3$). The free end of the pipe is subjected to linearly-decaying force pulses, where the initial force intensity falls within the range $f_0 \in [3, 30]$.

The deformation profiles of the pipe whip, and their time history, are presented in Fig. 10 and Fig. 11 for four values of $f_0 = [3, 5, 6, 10]$. The dimensionless plots on the left-hand side correspond to thick pipes (test case $T1$), and on the right-hand side to thin pipes (test case $T2$). Similar behaviours were observed between the test cases $T2$ and $T3$, therefore only the plots belonging to the case $T2$ are reported. The reference frame is positioned on the initial position of the tip, which is located on the right-hand side of each plot.

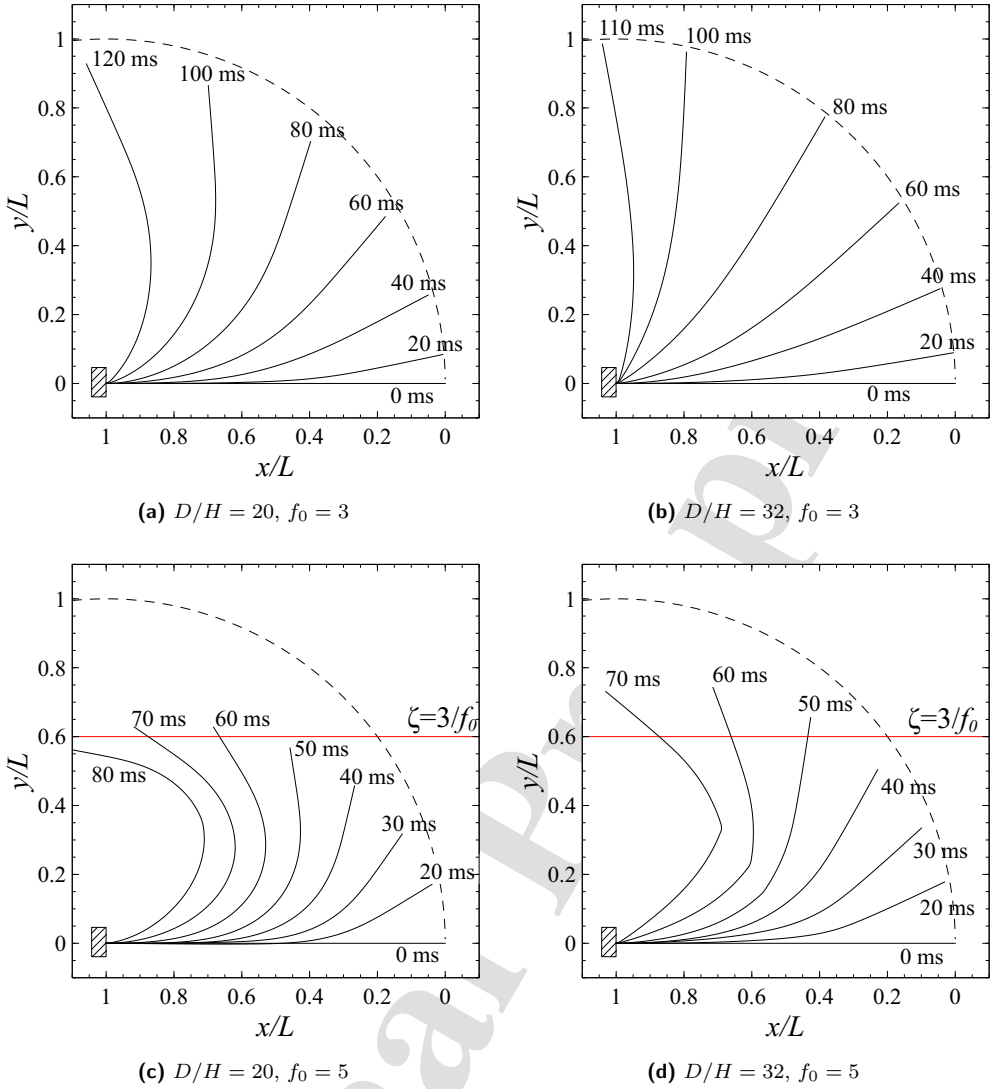

(a) $D/H = 20,\ f_0 = 3$ **(b)** $D/H = 32,\ f_0 = 3$

(c) $D/H = 20,\ f_0 = 5$ **(d)** $D/H = 32,\ f_0 = 5$

Figure 10: Dimensionless deformation profiles of thick and thin pipe whip ($D/H = 20$ and $D/H = 32$, respectively), subjected to orthogonal follower forces of initial intensity $f_0 = 3$ (a, b) and $f_0 = 5$ (c, d). The dimensionless vertical position is compared with the hazard zone predicted by the analytical RPP model, $\zeta = 3/f_0$. A circular arc with radius equal to the pipe length and centred in the fixed end is used to represent the maximum deformation range allowed.

As predicted by the analytical model of Sect. 3, when $f_0 = 3$, the pipes rotate about the root and the hazard zone reaches the maximum range allowed, equal to the pipe length. When $f_0 > 3$, a different deformation mechanism is observed, which is characterised by the formation of multiple plastic hinges. In these cases, the deformation range is reduced and is comparable to the extent of hazard zone $\zeta \approx \lambda = 3/f_0$.

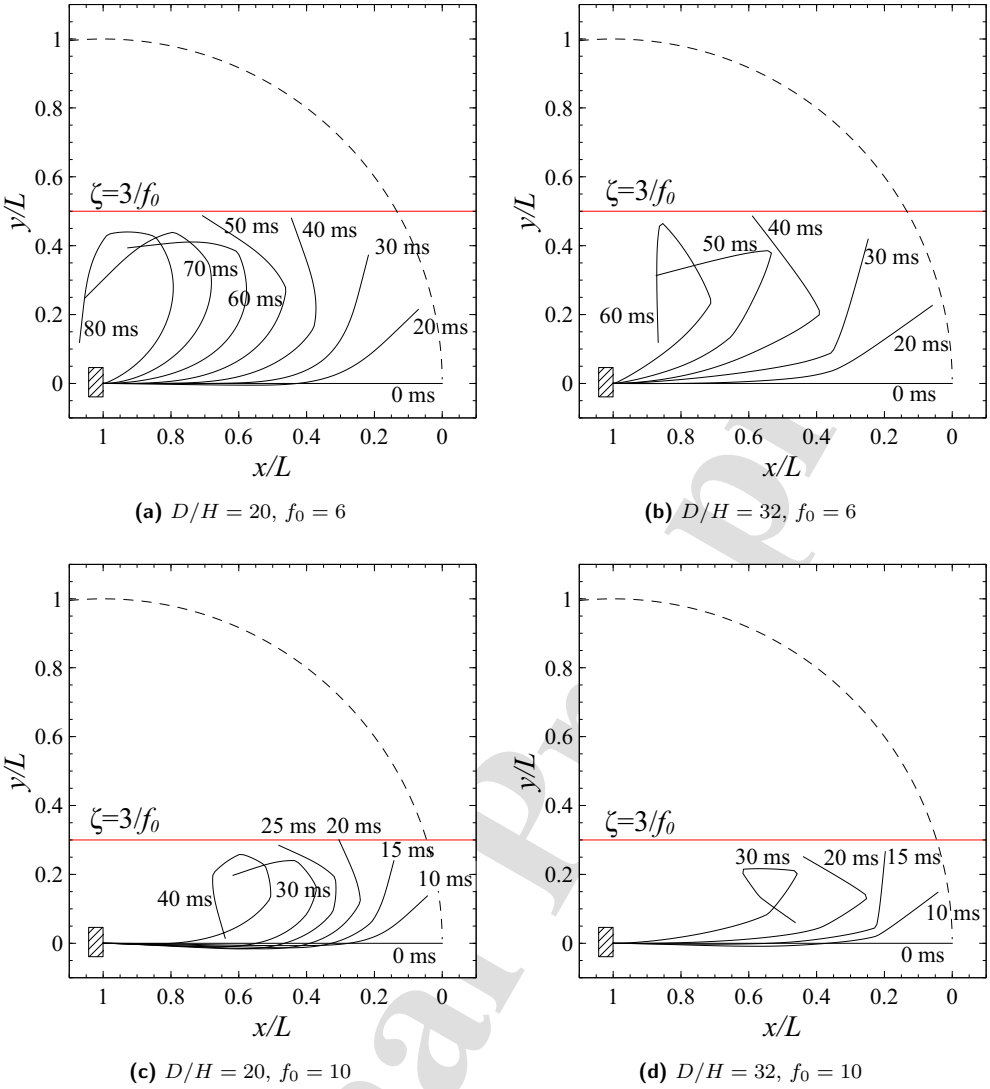

Figure 11: Dimensionless deformation profiles of thick and thin pipe whip ($D/H = 20$ and $D/H = 32$, respectively), subjected to orthogonal forces of initial intensity $f_0 = 6$ (a, b) and $f_0 = 10$ (c, d). The dimensionless vertical position is compared with the hazard zone predicted by the analytical RPP model, $\zeta = 3/f_0$. A circular arc with radius equal to the pipe length and centred in the fixed end is used to represent the maximum deformation range allowed.

Diverse mechanisms were observed numerically, depending on the loading intensity and the relative thickness of the pipe. In order of increasing load intensity, they are:

(i) *Cantilever mode* – when a stationary hinge develops at the root;

(ii) *Double-hinge mode* – when a plastic hinge develops along the pipe, followed by the formation of a secondary hinge at the root;

(iii) *Triple-hinge mode* – similar to the previous mode, characterised by the formation of three plastic hinges, the last being formed at the root. This mechanism is observed only for thin pipes;

(iv) *Self-intersecting mode* – when the pipe collapses on itself, forming a loop. Three or more plastic hinges develop along the pipe, but there is negligible rotation about the fixed end.

The self-intersecting pipe produces a significantly reduced hazard zone, thus decreasing the probability of impacting external bodies. However, the curvature is not always high enough to cause complete obstruction of the fluid flow [3, 25], leading to the uninterrupted release of the internal fluid, increasing the hazard of the system (e.g. temperature increase, release of chemicals, risk of explosion). When modelling the case of self-intersecting collapse, the simulation was stopped at the moment of self-contact, to avoid the use of a computationally expensive contact model. Loading intensities in the range $f_0 > 30$ are not considered here, as they are expected to cause deformations with a small hazard zone ($\zeta < 0.1$).

A more precise analysis of the formation and growth of plastic hinges is conducted by looking at the distribution of curvature along the pipe, as presented in Fig. 12 and Fig. 13. Initially, the deformation propagates from the free end as an elastic bending wave. It can be seen that, for all values of f_0, the segment adjacent to the free end stays in elastic conditions throughout the simulation. A small region of negative curvature forms at the fixed end as a consequence of the elastic properties of the beam. This is in agreement with the analytical observations of reverse bending from Stronge and Yu [9]. The relatively low value of negative curvature causes negligible deformation, which cannot be appreciated in the deformation profiles of Fig. 10 and Fig. 11. After no more than 20 ms the rest of the pipe starts deforming plastically, and the curvature goes above the yield value ($k_y/k_c = 0.03$ for thick pipes and $k_y/k_c = 0.08$ for thin pipes, according to the moment-curvature relation used). It is here assumed that plastic hinges form when the curvature exceeds the critical value $k/k_c \geq 1$.

Figure 12(a) and (b) show that, for $f_0 = 3$, as the deformation progresses, the curvature at the pipe's fixed end increases until it exceeds $k/k_c = 1$, and a plastic hinge forms at $x/L = 1$, in accordance to the *cantilever mode* identified in Fig. 10(a) and (b). As the force is increased ($f_0 = 5$), the *double hinge mode* is observed, with the first hinge forming at a distance $x/L \approx 0.5$ from the free end, and the second hinge forming at the root.

As the loading is increased further, Fig. 13, we assist at the formation of three or more hinges, eventually leading to the *self-intersecting* mode. Figure 13(c) and (d) highlight a fundamental difference in the collapse mechanism of relatively thick and thin pipes. In Fig. 13(c), the consecutive hinges are connected by regions with high levels of curvature, resulting in the formation of an extended plastic region, as observed in Fig. 11(c). Instead, in Fig. 13(d) plastic hinges are separated by regions of low curvature, resulting in the localised collapse mechanism of Fig. 11(d). These observations are coherent with what was observed experimentally in [3].

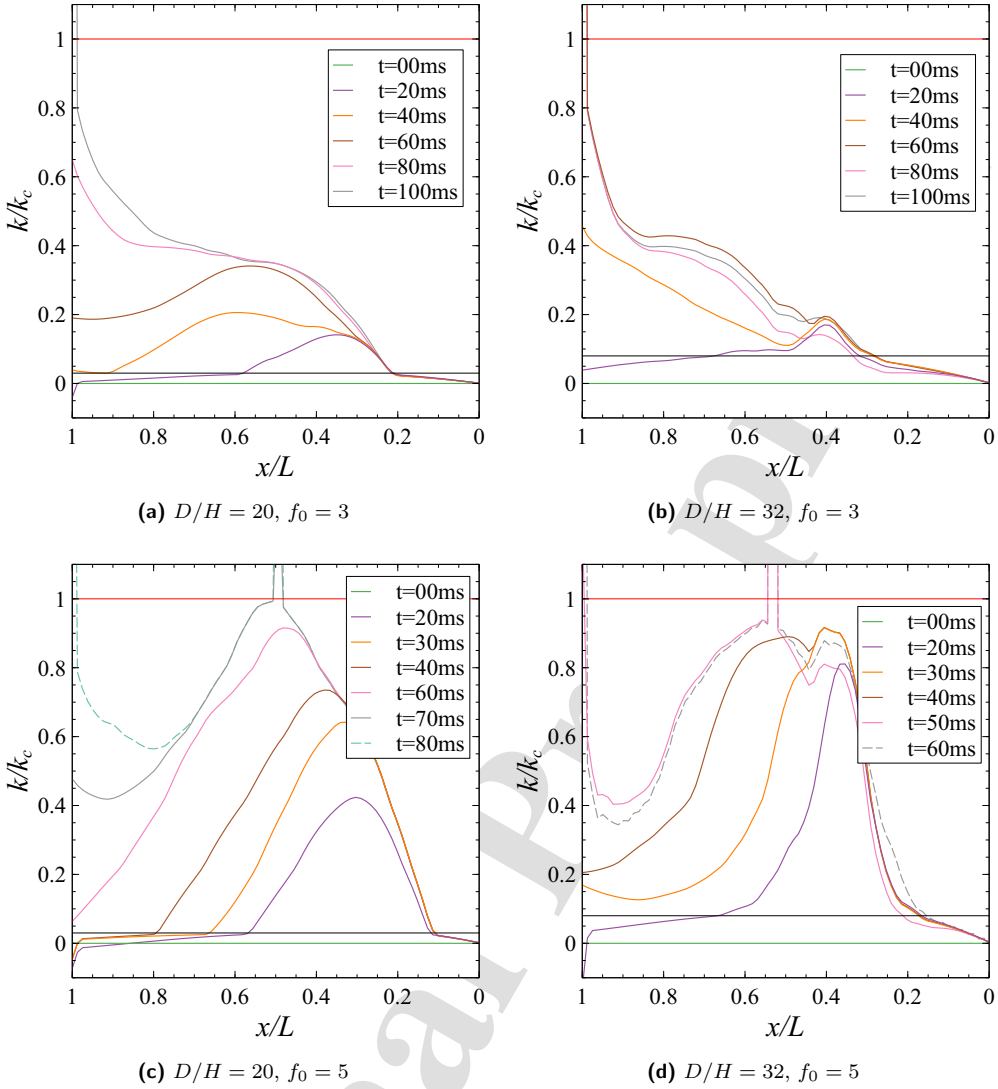

(a) $D/H = 20,\ f_0 = 3$ **(b)** $D/H = 32,\ f_0 = 3$

(c) $D/H = 20,\ f_0 = 5$ **(d)** $D/H = 32,\ f_0 = 5$

Figure 12: Time history of dimensionless curvature distributions along the pipes, k/k_c, for loading intensity $f_0 = 3$ and $f_0 = 5$. Black lines (—) indicate the yield point, red lines (—) indicate the critical point $k/k_c = 1$. Solid lines of different colours (—) indicate curvature distributions from the time $t = 0$ ms up to the moment of formation of a plastic hinge, while dashed lines (- -) are used in the time frames subsequent to plastic hinge formation.

325 The hinge position predicted by the analytical model, Sect. 3, at $t = 0$ s and $t = 0.2$ s (previously depicted in Fig. 5 with λ_0 and $\lambda(\tau)$, respectively), are compared with the numerical predictions in Fig. 14 for the three pipe geometries considered, $D/H = [20, 32, 40]$. Different symbols are used to highlight the first (λ_1), second (λ_2) and third (λ_3) plastic hinges, whereas the error bars indicate the length of the plastic region that is observed for thick pipes. Figures 14(a, b, c) show that the theoretical model of Eqs. (11) and

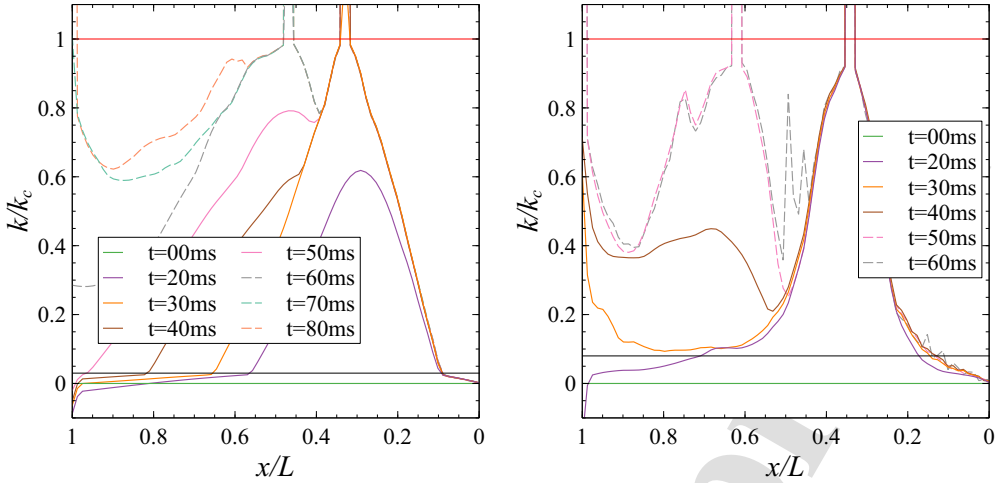

(a) $D/H = 20,\ f_0 = 6$ **(b)** $D/H = 32,\ f_0 = 6$

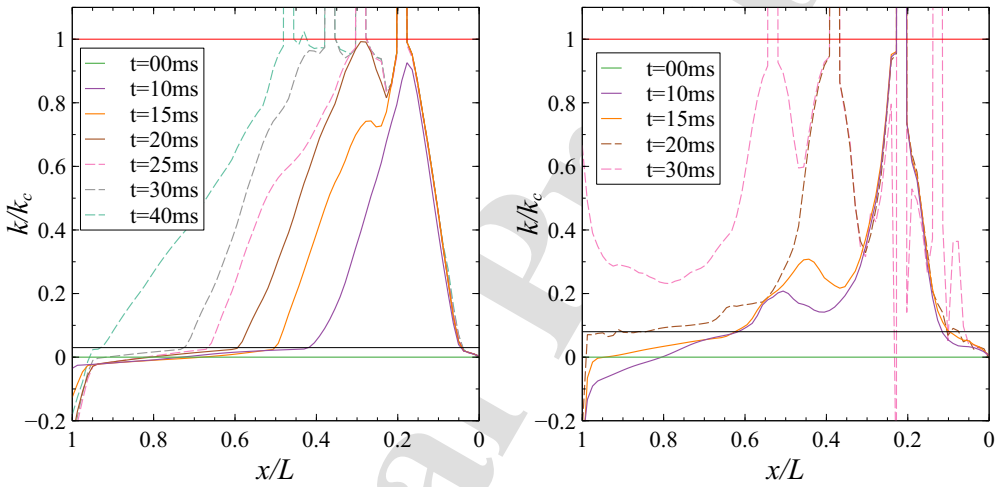

(c) $D/H = 20,\ f_0 = 10$ **(d)** $D/H = 32,\ f_0 = 10$

Figure 13: Time history of dimensionless curvature distribution along the pipes, k/k_c, for loading intensity $f_0 = 6$ and $f_0 = 10$. Black lines (—) indicate the yield point, red lines (—) indicate the critical point $k/k_c = 1$. Solid lines of different colours (—) indicate curvature distributions from the time $t = 0$ ms up to the moment of formation of a plastic hinge, while dashed lines (- -) are used in the time frames subsequent to plastic hinge formation.

(21) tends to over predict the λ_1 length, especially for the thick pipe. This phenomenon can be attributed to several causes. The analytical model allows rotation only at a single plastic hinge (a travelling hinge in the case of a decaying pulse), which is in disagreement with the observation of multiple hinges and extended plastic regions obtained numerically and from previous experiments [3, 25]. Furthermore, the analytical model fails to take into account elastic effects. Nevertheless, the theoretical model is in excellent agreement

335 with numerical predictions for the extent of the hazard zone, ζ, as reported in Fig. 14(d) and previously observed in Figs. 10 and 11.

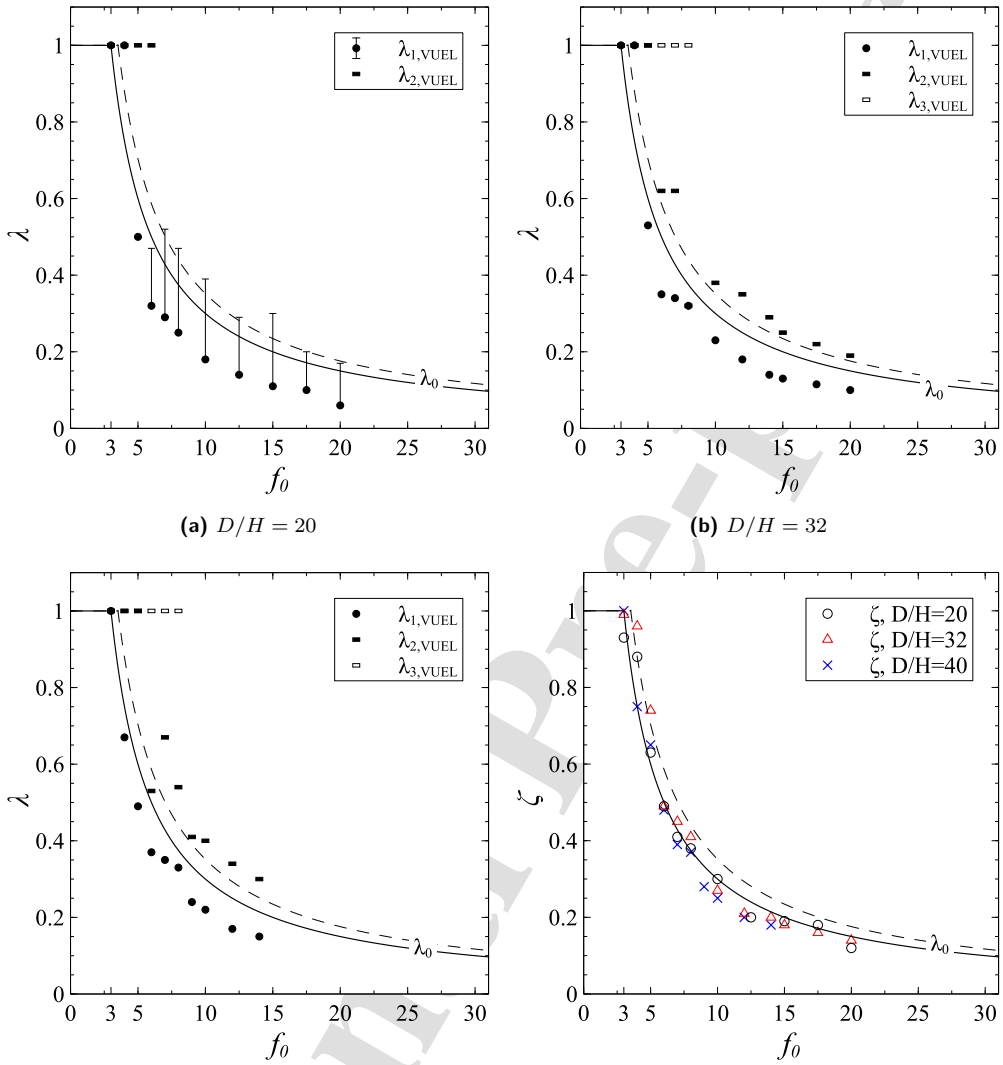

(a) $D/H = 20$ **(b)** $D/H = 32$

(c) $D/H = 40$ **(d)** Hazard zone ζ

Figure 14: Numerical predictions of the hinge position λ_i (a,b,c) and of the hazard zone ζ (d) reported as a function of the dimensionless follower force $f_0 \in [3, 30]$ to assess the influence of pipe geometry, $D/H = 20, 32, 40$, on the dynamic deformation response. The solid (—) and dashed (– –) curves represent the analytically-derived hinge position λ at time $t = 0.0$ s (λ_0) and $t = 0.2$ s, respectively.

Table 5: Values of pipe dimensions for the second parametric study on pipe whip, where each pipe has a concentrated mass m at its tip. All other parameters are unvaried from Table 4.

Test case	D/H	m (kg)	$\gamma = m/(\rho AL)$
$M1$	20	1.8	0.2
$M2$	32	1.4	0.2
$M3$	40	1700	1.1

5.2. Effect of concentrated tip mass

The second parametric study investigates the formation of plastic hinges and the extent of the hazard zone during the dynamic deformation of pipes that have an additional concentrated mass m at their free end, which aims to simulate the weight of a flange or connector. The values of concentrated mass for the test cases $M1$ and $M2$, reported in Table 5, are taken from [3]. The mass for test case $M3$ corresponds to that of a typical flange for high-pressure pipelines [34].

From the numerical results shown in Fig. 15, it can be observed that the presence of the concentrated tip mass has the effect of extending the range of f_0 in which the cantilever deformation mode occurs. In particular, this was the only mode of deformation observed for the test case $M3$ in the whole range of f_0 considered. For this reason, the plot of the case $M3$ results is omitted. In the test case $M1$, Fig. 15(a), a singular deformation mode takes place for $f_0 = 14$, in which the first plastic hinge forms at the fixed end ($\lambda = 1$), followed by the formation of a secondary hinge at $\lambda \approx 0.42$. At $f_0 = 15$, an abrupt transition between cantilever mode and self-intersecting mode is observed.

Numerical predictions of ζ for the two cases are shown in Fig. 15(a) and (b) as white circles and triangles, respectively. The results are compared with those obtained with the analytical model using Eq. (18) for $\lambda_0(\gamma = 0.2)$, and Eq. (22) for $\lambda(\tau = 1.17, \gamma = 0.2)$, that are reported in the figure with green solid and dashed lines, respectively. In both cases, the theoretical model provides a considerable underestimation of the plastic hinge position, compared to numerical observations. For this reason, the parametric study is repeated for different values of γ. The plot points in Fig. 16 indicate the hazard zone predicted for a pipe with $D/H = 32$ as a function of the dimensionless follower force range $f_0 \in [3, 30]$, loaded with a variable concentrated mass at its free end. The value of γ is increased until the only deformation mode observed in the force range is the cantilever mode.

The theoretical model of Eq. (18) is not capable of predicting accurately the hazard zone, therefore a parametric phenomenological relation is employed to fit the numerical data when the deformation mode deviates from the cantilever mode

$$\zeta = \frac{3}{f_0 - a_1 \gamma^{\, a_2}} + b_1 \gamma^{\, b_2} \, . \tag{25}$$

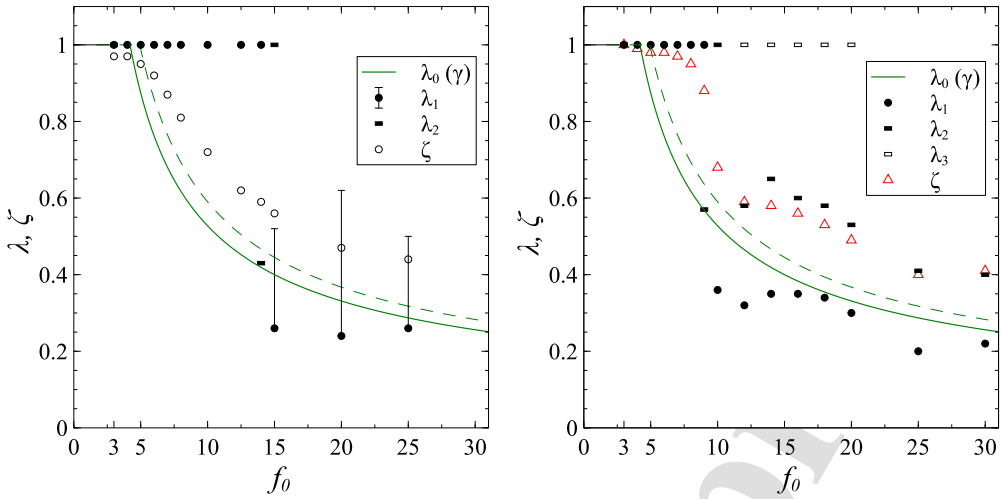

(a) $D/H = 20$ **(b)** $D/H = 32$

Figure 15: Numerical predictions of the hinge position λ_i and the hazard zone ζ reported as a function of the dimensionless follower force $f_0 \in [3, 30]$ for thick (a) and thin (b) pipe whip with a mass $\gamma = 0.2$ at its tip. The green solid (—) and dashed (– –) curves represent the analytically-derived hinge position λ at $\tau = 0$ (λ_0) and $\tau = 1.17$, respectively.

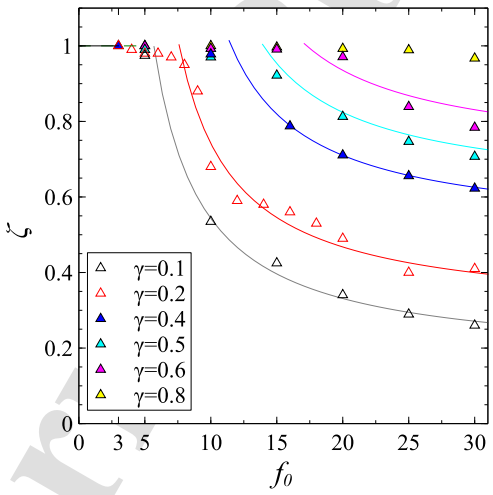

Figure 16: Numerical predictions of hazard zone ζ reported as a function of the dimensionless follower force $f_0 \in [3, 30]$ for thin pipe whip with $\gamma \in [0.1, 0.8]$. Solid lines represent the fitting curves using the model of Eq. (25).

The best-fit parameters found are $a_1 = 10.44, a_2 = 0.6968, b_1 = 1.057, b_2 = 0.8102$. The parametric model reduces to $\zeta = 3/f_0$ when $\gamma = 0$, which successfully predicts the hazard zone for both thick and thin pipes, as already demonstrated in Fig. 14(d).

6. Conclusion

A beam element code has been developed to study the inelastic dynamic response of pressurised pipes deforming in a whip-like motion under the influence of an intense follower force generated by the escape of fluids caused by a sudden guillotine break. The developed user element employs a corotational kinematic formulation and a constitutive relationship that idealises the cross-sectional collapse mechanisms of tubes in bending. The pipes flexural constitutive behaviour has been obtained through numerical experiments of pipes in bending, which highlighted the existence of three dimensionless groups, namely π_1, π_2 and π_3, defining dimensionless moment-curvature master curves for thick and thin pipes.

The beam user element has been implemented in a commercial FE software through a user element subroutine VUEL and it has been used to perform FE simulations that model the in-plane deformation of slender thick and thin pipe whips. The numerical results have been compared with experimental measurements performed by Reid et al. [3], analytical predictions from a rigid-perfectly plastic beam model, and finite element results employing shell elements. It has been proven that the developed corotational beam element correctly captures the experimental and numerical deformation mechanisms and the pipe hazard zone, whilst reducing by two orders of magnitude the computational time required by simulations employing shell elements. Additionally, modelling the deformation of pipes with VUEL elements has the practical advantage of simplifying the analysis of the deformation modes that follow the pipe collapse and improving the accuracy in identifying the plastic hinges. In a model employing shell elements, the variation in curvature during the deformation needs to be calculated by integrating the rotation of all elements at a given cross-section, and comparing it to the rotation of the longitudinal axis. In the employed finite element software, this measurement of the curvature can only be performed at the end of the analysis on predetermined sites along the pipe, which must be defined before the analysis, thus limiting the capability of analysing with accuracy the collapse mechanism and the extension of plastic hinges. On the contrary, using the VUEL elements allows to readily measure the curvature variation, and thus the collapse, in each element throughout the analysis. A possible limiting factor in the accurate identification of plastic hinges with the VUEL is the element size, which is recommended to be smaller than the pipe's external diameter. Employing the VUEL elements has allowed the characterisation of the diverse deformation mechanisms described in Sect. 5.1.

Furthermore, the beam element code has been used to perform parametric studies to analyse the effects of load intensity, cross-sectional geometry and concentrated tip mass on the plastic hinge formation, the extension of the dangerous pipe area of influence and the identification of different deformation mechanisms, including cantilever mode, double or triple hinge modes, and self-intersecting mode. These studies have also shown that the analytical rigid-perfectly plastic model provides conservative predictions for the formation of plastic hinges and defines with satisfying accuracy the hazard zone of pipe whip only in the absence of heavy tip flanges. On the contrary, the results obtained with the developed user element enable a fast and

accurate prediction of the hazard area, thus being effective tools for the design of pipe whip restraint devices.

The current work can be improved by including in the constitutive model the effects of strain rate and the interaction between axial forces and bending moment, which are currently neglected. Additionally, the development of a three-dimensional element to simulate the out-of-plane deformation of initially bent pipes under simultaneous bending and twisting is part of an ongoing study. Lastly, the loading caused by the fluid jet was modelled as a concentrated follower force, and its intensity was assigned by a pre-determined decaying pulse calculated from experiments. In a real-life pipe whip scenario, the initial load intensity is determined by the fluid pressure, and its evolution is dictated by the cross-sectional collapse as the pipe deforms. Future improvements to the element code should focus on the development of a subroutine that calculates the decrease of the force intensity caused by the reduction of the inner cross-sectional area, which is, in turn, a function of the curvature.

Acknowledgement

P.J.T. wishes to acknowledge the funding awarded by QinetiQ-UK (Mr Robert Ball – Structures & Survivability, Platform Design and Life Support IDT) which was used to support D.S.M. in the form of a PhD studentship. F.B. acknowledges support from the EU H2020-MSCA-ITN-2020-LIGHTEN-956547.

References

[1] G. Lu, T. Yu, Energy Absorption of Structures and Materials, CRC Press, 2003. doi:10.1201/9780203484128.

[2] K. Song, Y. Long, C. Ji, F. Gao, H. Chen, Experimental and numerical studies on the deformation and tearing of x70 pipelines subjected to localized blast loading, Thin-Walled Structures 107 (2016) 156–168. doi:https://doi.org/10.1016/j.tws.2016.03.010.

[3] S. R. Reid, T. X. Yu, J. L. Yang, G. G. Corbett, Dynamic elastic-plastic behaviour of whipping pipes: Experiments and theoretical model, Int. J. Impact Eng. 18 (7-8) (1996) 703–733. doi:10.1016/s0734-743x(96)00034-6.

[4] X. Luo, W. Du, C. Wang, C. Liu, J. Yang, P. Li, J. Zhang, Experimental study of u-bolt pipe whip restraint: Deformation process and energy absorbing, in: ASME Int. Mech. Eng. Congr. Expo. Proc., Vol. 14-2015, ASME, 2015, p. V014T08A007. doi:10.1115/IMECE2015-50848.

[5] A. R. Telford, Impact assessment in the uk nuclear power industry: An overview of the r3 impact assessment procedure, Int. J. Press. Vessel. Pip. 87 (9) (2010) 520–529. doi:10.1016/j.ijpvp.2010.07.005.

[6] K. Fullard, D. Thomas, S. Wicks, The r3 impact assessment procedure for nuclear power plant structures, in: Trans. SMiRT 11 Conf., Vol. J05, 1991, pp. 81–86.

[7] D. S. Queener, Reports, standards, and safety guides, Nucl. Saf. 37 (4) (1996) 391–395.

[8] M. R. Baum, The rupture of high pressure pipework: The influence of pipeline geometry on in-plane pipewhip, J. Loss Prev. Process Ind. 9 (2) (1996) 147–159. doi:10.1016/0950-4230(96)00004-6.

[9] W. J. Stronge, T. Yu, Dynamic Models for Structural Plasticity, Springer London, London, 1993. doi:10.1007/978-1-4471-0397-4.

[10] S. R. Reid, B. Wang, Large-deflection analysis of whipping pipes. i: Rigid, perfectly-plastic model, J. Eng. Mech. 121 (8) (1995) 881–887. doi:10.1061/(ASCE)0733-9399(1995)121:8(881).

[11] S. R. Reid, T. Yu, J. L. Yang, Response of an elastic, plastic tubular cantilever beam subjected to a force pulse at its tip-small deflection analysis, Int. J. Solids Struct. 32 (23) (1995) 3407–3421. doi:10.1016/0020-7683(94)00314-M.

[12] I. Micheli, P. Zanaboni, An analytical validation of simplified methods for the assessment of pipe whip characteristics, in: Trans. 17th Int. Conf. Struct. Mech. React. Technol. (SMiRT 17), 2003, pp. 1–8.

[13] 3DS Dassault Systèmes, SIMULIA Abaqus 2017 Documentation, Dassault Systèmes, Providence, RI, 2016.

[14] L. Zeng, L. G. Jansson, Y. Venev, On pipe elbow elements in abaqus and benchmark tests, in: Proc. ASME 2014 Press. Vessel. Pip. Conf., no. 10, American Society of Mechanical Engineers, 2014. doi:10.1115/PVP2014-28920.

[15] T. Belytschko, B. J. Hsieh, Non-linear transient finite element analysis with convected co-ordinates, Int. J. Numer. Methods Eng. 7 (3) (1973) 255–271. doi:10.1002/nme.1620070304.

[16] M. A. Crisfield, A consistent co-rotational formulation for non-linear, three-dimensional, beam-elements, Comput. Methods Appl. Mech. Eng. 81 (2) (1990) 131–150. doi:10.1016/0045-7825(90)90106-V.

[17] M. Crisfield, G. Moita, A unified co-rotational framework for solids, shells and beams, Int. J. Solids Struct. 33 (20) (1996) 2969–2992. doi:https://doi.org/10.1016/0020-7683(95)00252-9.

[18] C. A. Felippa, B. Haugen, A unified formulation of small-strain corotational finite elements: I. theory, Comput. Methods Appl. Mech. Eng. 194 (21-24 SPEC. ISS.) (2005) 2285–2335. doi:10.1016/j.cma.2004.07.035.

[19] T.-N. Le, J.-M. Battini, M. Hjiaj, Efficient formulation for dynamics of corotational 2d beams, Comput. Mech. 48 (2) (2011) 153–161. doi:10.1007/s00466-011-0585-6.

[20] T.-N. Le, J.-M. Battini, M. Hjiaj, A consistent 3D corotational beam element for nonlinear dynamic analysis of flexible structures, Comput. Methods Appl. Mech. Eng. 269 (2014) 538–565. doi:10.1016/j.cma.2013.11.007.

[21] H. Cho, H. Joo, S. Shin, H. Kim, Elastoplastic and contact analysis based on consistent dynamic formulation of co-rotational planar elements, Int. J. Solids Struct. 121 (2017) 103–116. doi:https://doi.org/10.1016/j.ijsolstr.2017.05.019.

[22] R. M. Brannon, Frame indifference, in: Rotation, Reflection, and Frame Changes, 2053-2563, IOP Publishing, 2018, pp. 19–1 to 19–49. doi:10.1088/B978-0-7503-1454-1.00019-1.

[23] R. Courant, K. Friedrichs, H. Lewy, On the partial difference equations of mathematical physics, IBM J. Res. Dev. 11 (2) (1967) 215–234. doi:10.1147/rd.112.0215.

[24] D. Schiano Moriello, Failure of impulsively loaded thin-walled pipes and plates, Ph.D. thesis, University College London (2021).

[25] Hardening-softening behaviour of circular pipes under bending and tension, Int. J. Mech. Sci. 36 (12) (1994) 1073–1085. doi:10.1016/0020-7403(94)90059-0.

[26] S. R. Reid, J. L. Yang, Pipe whip: In-plane whipping of bent cantilever pipes, J. Press. Vessel Technol. 120 (2) (1998) 170. doi:10.1115/1.2842236.

[27] N. K. Prinja, N. R. Chitkara, Finite-element analyses of post-collapse plastic bending of thick pipes, Nucl. Eng. Des. 91 (1) (1986) 1–12. doi:10.1016/0029-5493(86)90179-2.

[28] T. Yu, J. Yang, S. Reid, Deformable body impact: dynamic plastic behaviour of a moving free–free beam striking the tip of a cantilever beam, Int. J. Solids Struct. 38 (2) (2001) 261–287. doi:https://doi.org/10.1016/S0020-7683(00)00019-6.

[29] D. Karagiozova, M. Alves, Transition from progressive buckling to global bending of circular shells under axial impact—part i: Experimental and numerical observations, Int. J. Solids Struct. 41 (5) (2004) 1565–1580. doi:https://doi.org/10.1016/j.ijsolstr.2003.10.005.

[30] F. Bosi, A. Schlothauer, C. Leclerc, S. Pellegrino, Cure-induced deformation of ultra-thin composite laminates, in: 2018 AIAA/ASCE/AHS/ASC Structures, Structural Dynamics, and Materials Conference, 2018, p. 2241. doi:https://doi.org/10.2514/6.2018-2241.

[31] G. N. Nurick, G. C. Shave, The deformation and tearing of thin square plates subjected to impulsive loads - an experimental

study, Int. J. Impact Eng. 18 (1) (1996) 99–116. doi:10.1016/0734-743X(95)00018-2.

[32] D. Schiano Moriello, F. Bosi, R. Torii, P. Tan, Failure and detachment path of impulsively loaded plates, Thin-Walled Structures 155 (2020) 106871. doi:10.1016/j.tws.2020.106871.

[33] S. R. Reid, M. Aleyaasin, B. Wang, Out-of-plane pipe whip for a bent cantilever pipe: Comparison between experiment and fem models, J. Appl. Mech. Trans. ASME 79 (1) (2012) 011005. doi:10.1115/1.4004712.

[34] Standard ASME B36. 19M-2004: Stainless Steel Pipe, American Society of Mechanical Engineers, 2004.

Declaration of interests

☒ The authors declare that they have no known competing financial interests or personal relationships that could have appeared to influence the work reported in this paper.

☐ The authors declare the following financial interests/personal relationships which may be considered as potential competing interests: